

Article

Effects of Thermal Cycle and Ultraviolet Radiation on 3D Printed Carbon Fiber/Polyether Ether Ketone Ablator

Farhan Abdullah ^{1,*} , Kei-ichi Okuyama ², Akito Morimitsu ¹ and Naofumi Yamagata ¹

¹ Department of Applied Science for Integrated Systems Engineering, Kyushu Institute of Technology, 1-1 Sensui, Tobata, Kitakyushu, Fukuoka 804-8550, Japan; p111047a@mail.kyutech.jp (A.M.); o111048n@mail.kyutech.jp (N.Y.)

² Department of Aerospace Engineering, College of Science and Technology, Nihon University, 7-24-1 Narashinodai, Funabashi, Chiba 274-8501, Japan; okuyama.keiichi@nihon-u.ac.jp

* Correspondence: abduallah.farhan835@mail.kyutech.jp

Received: 27 May 2020; Accepted: 6 July 2020; Published: 8 July 2020



Abstract: The extreme heating environment during re-entry requires an efficient heat shield to protect a spacecraft. The current method of manufacturing a heat shield is labor intensive. The application of 3D printing can reduce cost and manufacturing time and improve the quality of a heat shield. A 3D printed carbon fiber/polyether ether ketone (CF/PEEK) composite was proposed as a heat shield material. The aim was to develop a heat shield and the structural member as a single structure while maintaining the necessary recession resistance. Test samples were exposed to thermal cycles and ultraviolet (UV) radiation environment. Subsequently, a tensile test was performed to evaluate the effect of thermal cycle and UV radiation on the mechanical properties. The sample's recession performance and temperature behavior were evaluated using an arc heated wind tunnel. Exposure to thermal cycle and UV radiation have limited effect on the mechanical properties, recession behavior and temperature behavior of 3D CF/PEEK. Results from the arc heating test showed an expansion of the sample surface and better recession resistance than other existing ablator materials. Overall, 3D CF/PEEK has excellent recession resistance while maintaining mechanical properties when exposed to high temperature, thermal cycle and UV radiation.

Keywords: 3D printing; additive manufacturing; ablation; arc-heated; carbon fiber; heat shield; polyether ether ketone (PEEK); re-entry; thermal cycle; ultraviolet

1. Introduction

Spacecraft are exposed to an extreme heating environment when entering Earth or another planetary atmosphere. An efficient thermal protection system (TPS), hereafter referred to as a heat shield, must be used to minimize heat conducted into the spacecraft. Moreover, a heat shield needs to have excellent specific strength, specific rigidity and high resistance to shear loads caused by aerodynamic loading to the surface [1]. Heat shields can be divided into reusable and ablative heat shields [2]. Composite ablative heat shield materials consist of a resin and reinforcing material such as carbon fiber.

The ablative heat shield provides thermal protection through the process of ablation. The resin in the ablator undergoes pyrolysis reaction resulting in the release of pyrolysis gas and the carbonization of the resin while the carbon remains. A porous char layer is formed due to the carbonized resin. Pyrolysis gas percolates through the char surface and block incoming heat at the surface. At the same time, heat is absorbed when the pyrolysis gas percolates through the char layer. A thermochemical

process such as oxidation, sublimation, melting or vaporization and a mechanical process such as spallation cause the recession of the char layer [3].

The ablation process occurs in three modes. The first mode is the rate-controlled oxidation which occurs approximately below 1230 °C. The term rate refers to the rate for the carbon and oxygen chemical reaction. The second mode occurs between 1230 and 2730 °C and is termed as diffusion-controlled oxidation. The degradation rate is limited by the oxygen diffusion rate into the surface. The third mode occurring above approximately 2730 °C is termed as sublimation. The sublimation of carbon occurs during the third mode [4].

The current method of manufacturing heat shield is labor intensive, resulting in high manufacturing cost, long manufacturing time and quality issues. Moreover, most heatshields have gaps and seams which can increase the risk of accidents during re-entry. Recently, 3D printing or additive manufacturing (AM) technology has matured enough for application in the aerospace industry [5]. The European Space Agency has manufactured 3D printed PEEK structures for CubeSat. The unique feature was the embedded electrical lines inside the PEEK structure [6]. The Group of Astrodynamics for the Use of Space Systems in Italy developed the TuPOD 3U CubeSat. TuPOD was manufactured completely by 3D printing using Windform X2, a proprietary material by CRP USA [7]. The application of 3D printing in the manufacturing of heat shield has the potential to reduce cost and manufacturing time and improve quality by including high accuracy in manufacturing [8]. Moreover, 3D printing allows the ability to manufacture monolithic or one-piece heat shield, thus reducing gaps and seams. Recently, the National Aeronautics and Space Administration (NASA) conducted preliminary research regarding 3D printed TPS. NASA applied thermoset resin mixture printing to manufacture the test pieces [8].

Before re-entry, the long duration exposure of the ablator materials to the low Earth orbit (LEO) environment may affect the thermal and mechanical performance of the ablator. Exposure to thermal cycles causes the temperature to vary between -160 and $+120$ °C when a satellite passes from direct sunlight into Earth shadow [9]. This process repeats continuously throughout the satellite mission life. The thermal cycle can affect the mechanical properties of composites such as tensile strength and Young's modulus [10]. The ultraviolet (UV) wavelength in LEO is between 0.1 and 0.4 μm (100–400 nm) [11]. The shorter is the wavelength, the greater is the UV energy. The mean energy possesses by vacuum ultraviolet (VUV) and UV-C is 214.5 and 122.6 Kcal/mole, respectively. Therefore, VUV and UV-C have the potential to break several chemical bonds [12]. A previous study described that UV radiation with a spectrum less than or equal to 250 nm is the dominant contributor for material degradation [13]. UV radiation causes both chain scission and crosslinking of polymers, thus affecting the mechanical properties [14]. However, there is limited information on the effect of thermal cycle and UV radiation on the thermal performance of composite ablators.

In this work, an ablator material using 3D printed carbon fiber/polyether ether ketone (CF/PEEK), hereafter referred to as 3D CF/PEEK, is proposed as a new material for a heat shield. The aim is to propose a heat shield that can incorporate the structural member and heat shield section as a single structure while maintaining the necessary recession resistance. Test samples were exposed to thermal cycles and ultraviolet (UV) radiation environment. The effects of thermal cycle and UV radiation on tensile strength and Young's modulus of the samples were evaluated using a tensile test. Further, the 3D CF/PEEK was exposed to a high-temperature environment in an arc heated wind tunnel for evaluation of surface and in-depth temperature response and recession resistance. A comparison with existing ablator materials was performed to determine the performance of 3D CF/PEEK compared to other ablator materials.

2. Materials and Methods

2.1. Materials

A 3D CF/PEEK composite developed by AGC Inc. (Tokyo, Japan) was used as the ablator material. CF/PEEK composite is a high-performance carbon fiber composite made of carbon fiber as reinforcement

material with PEEK as the matrix. PEEK is a semi-crystalline thermoplastic polymer. CF/PEEK can be an ideal material for use as a spacecraft material due to low outgassing properties, good resistance to space sourced radiation and good toughness property [9]. The 3D CF/PEEK was printed using Arevo laser-based direct energy deposition (DED) 3D printer (Arevo, CA, USA). Laser-based DED uses a laser to melt deposited material in the form of wire or filament. The filament is then compressed using a compaction roller to bond it to the previous layer or build plate. The DED process allows in-situ consolidation of parts. Figure 1 shows the laser-based DED process. Arevo 3D printer is capable of depositing materials in any orientation by using a six-axis 3D printing platform [15].

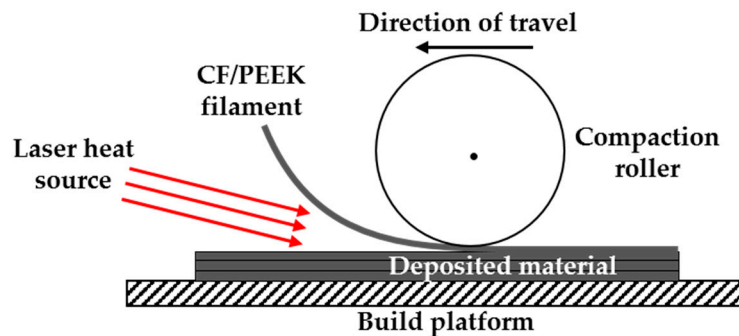


Figure 1. Illustration of the laser-based DED process [15].

Continuous carbon fiber impregnated with PEEK resin was used to make the filament. The fiber volume fraction is 56.5%. Two types of samples were manufactured: one for tensile test and another for arc heating test. The tensile test samples were cut from panels with (0/90/0) fiber layup direction. The arc heating test samples were cut from panels with (0/90)_S fiber layup direction. The type and dimension of the samples are listed in Table 1. Figures 2 and 3 show the computer-aided drawing (CAD) and actual picture of tensile and arc heating test samples, respectively.

Table 1. Sample types and dimensions for tensile and arc heating test.

Type of Test	Length (mm)	Width/Diameter (mm)	Thickness (mm)	Fiber Lay-up
Tensile test	150	20	2	(0/90/0)
Arc heating test	-	20	30	(0/90) _S

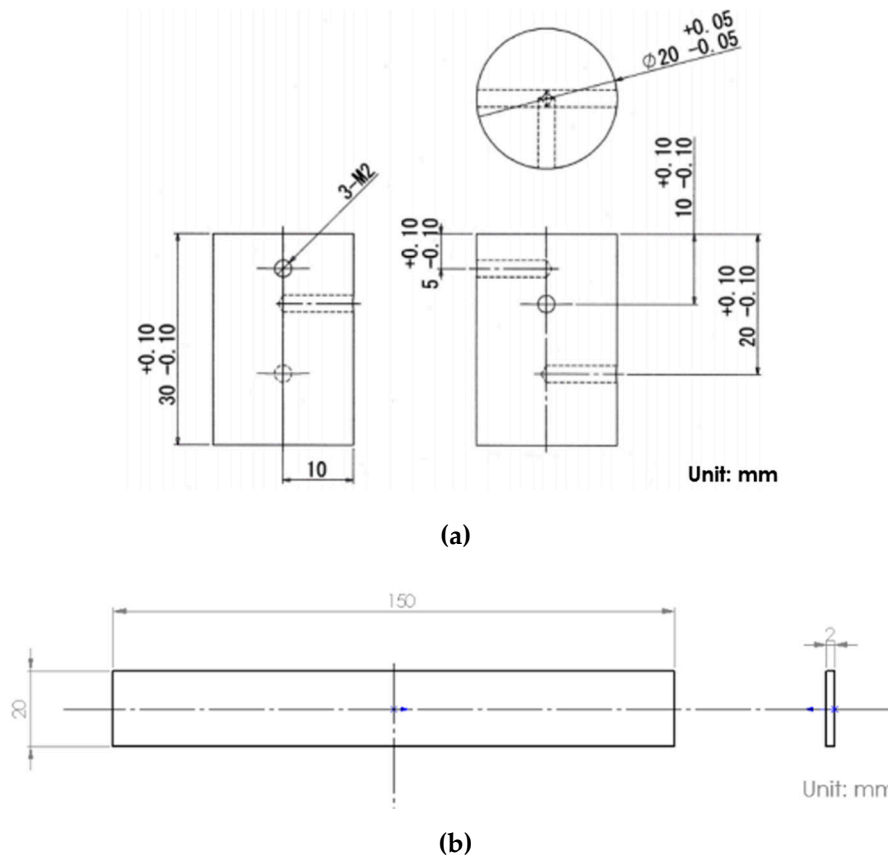


Figure 2. CAD drawing of test samples: (a) arc heating test sample with the position of holes for placement of thermocouples; and (b) tensile test sample.



(a)



(b)

Figure 3. Actual test samples: (a) side view of arc heating test sample; and (b) top view of the tensile test sample.

2.2. Exposure to Thermal Cycle

Long duration exposure to thermal cycles can affect the properties of 3D CF/PEEK. The large number of thermal cycles that the satellite will experience during a typical mission makes it difficult to perform real-time testing. The solution is to perform thermal cycle exposure at accelerated levels.

According to previous studies, thermal cycles can make a crack in carbon fiber reinforced plastic (CFRP) and carbon fiber reinforced thermoplastic (CFRTP), which leads to a change in mechanical properties [16,17]. This change can affect ablator performance during re-entry into the atmosphere.

The Coffin–Manson model is used to relate field usage to accelerated test conditions [18,19]. This is a simple model used for estimating the temperature cycle acceleration factor. Reasonably estimating the acceleration factor depends on the failures being caused by fatigue, subject to the Coffin–Manson law for cyclic strain versus the number of cycles to failure as shown in Equation (1) [18,20]:

$$\Delta\varepsilon_p N_f^\alpha = c \quad (1)$$

where $\Delta\varepsilon_p$ is the plastic strain amplitude, N_f is the number of cycles to failure, α is the fatigue ductility exponent and c is the material constant. When applied to an accelerated thermal cycling sequence, Equation (1) can be re-written to define the acceleration factor of the test as Equation (2) [18,20]:

$$AF = (\Delta T_{test} / \Delta T_{use})^m \quad (2)$$

where AF is the acceleration factor, ΔT_{test} is the temperature cycle test range, ΔT_{use} is the nominal temperature change in the field and m is the Coffin–Manson exponent. According to previous studies, the Coffin–Manson exponent for carbon fiber composites is approximately 6 [20].

There were two types of samples exposed to thermal cycle. The first type was for the tensile test while the second type was for arc heating test. The “Despatch 935E-1-4-120” (Despatch Industries, Minneapolis, USA) was used to create the thermal cycle conditions. Figure 4 shows the thermal cycle chamber. Table 2 shows the specification of the thermal cycle chamber.



Figure 4. The thermal cycle chamber used for exposing the tensile test and arc heating test samples to various numbers of thermal cycles.

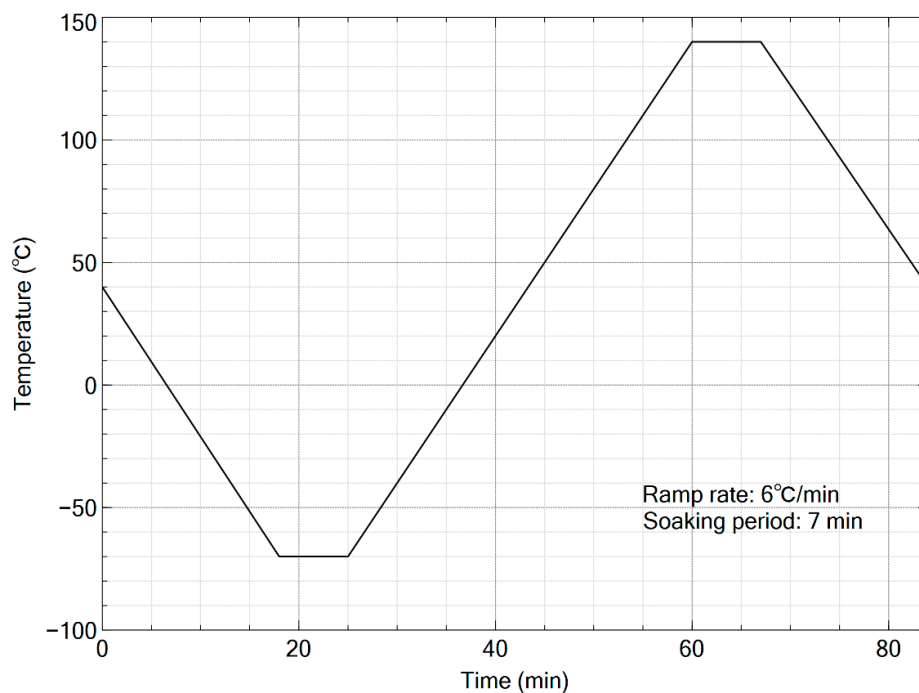
Table 2. Main specification of the thermal cycle chamber.

Specification	Description
Size (mm)	440 width × 480 depth × 500 height
Ultimate Vacuum (Pa)	Room pressure
Shroud temperature (°C)	−190 to 200 °C
Maximum test sample size (mm)	350 width × 250 depth × 200 height
Heating rate	40–100 °C: 6 °C/min, 40–200 °C: 19 °C/min 40–260 °C: 31 °C/min

An accelerated thermal cycle condition was performed for a temperature range between -70 and 140 °C. The thermal cycle involved heating in air and cooling using liquid nitrogen. The ΔT_{test} is -70 to 140 °C and the ΔT_{use} is -40 to 50 °C. The ΔT_{use} was based on a previous microsatellite external structure temperature measurements [21]. The equivalent number of thermal cycles in LEO orbit was calculated based on the assumption that the orbital period was equivalent to the International Space Station (ISS) orbital period of approximately 90 min [22]. The number of thermal cycles for the ground test was calculated using Equation (2). The calculated number of thermal cycles is shown in Table 3. Table 3 also shows the number of samples exposed to each thermal cycle condition. The heating and cooling rate or ramp rate was approximately 6 °C/min. The soaking period was 7 min to allow uniform distribution of heat over each test sample. The profile for one thermal cycle is shown in Figure 5.

Table 3. The number of tensile and arc heating test samples exposed to different thermal cycle conditions.

Mission Life (months)	Number of Thermal Cycles in Ground Test	Equivalent Number of Thermal Cycles in Orbit	Number of Samples Per Test Type	
			Tensile Test	Arc Heating Test
6	17	2800	2	2
9	26	4200	2	2
12	35	5600	2	2

**Figure 5.** Temperature profile for thermal cycle exposure.

2.3. Exposure to Ultraviolet Radiation

Two types of samples were exposed to different amounts of UV fluence. The first type was for tensile test purposes while the second type was for arc heating test. A UV chamber without a thermal vacuum was used for UV irradiation (WorldJB, Taito, Japan). A fluorescent lamp was used to provide UV irradiation with a wavelength of 253.7 nm, which is in the UV-C wavelength range (G6T5, Sankyo-Denki, Kanagawa, Japan). The test condition is shown in Table 4. A previous study has shown that UV degradation can be affected by temperature [23]. Therefore, the sample temperature was set to 50.0 °C to simulate UV degradation in space, which is the maximum temperature based on a thermal simulation of a small satellite in LEO. Table 5 shows the list of samples exposed to UV radiation.

Table 4. UV irradiation conditions.

Type of Test	UV Fluence (ESD)
Wavelength (nm)	253.7
UV fluence (ESD)	15, 30, 45
UV intensity (W/m ²)	20.5
Pressure in UV chamber (Pa)	1.013×10^5
Sample temperature (°C)	50.0

Table 5. List of samples exposed to thermal cycle.

UV Fluence (ESD ¹)	Number of Samples Per Test Type	
	Tensile Test	Arc Heating Test
15	2	2
30	2	2
45	2	2

¹ ESD refers to Equivalent Solar Day.

2.4. Tensile Test Method

Tensile tests were conducted after the test samples were exposed to the thermal cycle and UV radiation. The tensile test was performed by Agne Technical Center Co. Ltd. (Tokyo, Japan). The tensile properties were measured using a universal testing machine at room temperature. The tensile test procedure was based on the ASTM D3039 standard. The tensile test was conducted using 14 test samples. Two samples were pristine samples referred to as the base sample. Six samples were previously exposed to the thermal cycle while the remaining six samples were previously exposed to UV radiation. Table 6 shows the number of samples for each exposure condition. The applied displacement rate was 1 mm/min. The grip distance was 50 mm. The amount of strain was measured using the KFGS-5-120-C1-11 (Kyowa, Tokyo, Japan) strain gauge with a gauge length of 5mm. The Young's modulus calculation range was between 0.05% and 0.25% of the longitudinal strain.

Table 6. List of sample types for tensile tests.

Environment	Number of Test Samples
Base sample	2
2800 thermal cycles	2
4200 thermal cycles	2
5600 thermal cycles	2
15 ESD UV fluence	2
30 ESD UV fluence	2
45 ESD UV fluence	2

2.5. Arc Heating Test Method

Arc heating test was conducted after ablator samples were exposed to the thermal cycle and UV radiation. The ablator samples were exposed to high-temperature flow using an arc heated wind tunnel located in Japan Aerospace Exploration Agency (JAXA) Institute of Space and Aeronautical Science (ISAS) in Sagami-hara, Japan. Figure 6 shows the arc heated wind tunnel in ISAS. The distance between the wind nozzle and the sample surface was 100 mm. The heat flux varied between 5.0 and 14.2 MW/m². The heating duration was 10 s for 14.2 MW/m² heat flux and 20 s for 5.0 MW/m² heat flux. The lower heating duration for 14.2 MW/m² was due to a conservative approach for the ablator test. To our knowledge, this is the first time that a 3D CF/PEEK material was evaluated as a heat shield material, thus being exposed to high-temperature flow. Therefore, the initial plan was to have a preliminary assessment of the effects of high heat flux on 3D CF/PEEK as a potential heat shield material. Future test plans under consideration will incorporate a gradual increase in the heating duration. The gas flow used during the heating test was air. Table 7 shows the test conditions for the arc heating test. The surface temperature was measured using an infrared thermometer or pyrometer. The thermometer has a sensor that detects the infrared radiation on the sample surface. A type-K thermocouple was used to measure the internal temperature of the sample. The internal temperature was measured at 5, 10 and 20 mm from the sample surface. Figure 7 shows the location of each thermocouple within the sample. A Bakelite casing acts as a heat insulator to house each sample. The Bakelite tube was wrapped with glass cloth to reduce lateral heating of the sample and simulate one-dimensional heating. The purpose of the one-dimensional heating was to facilitate future comparison between ground test and a one-dimensional numerical analysis of the ablator performance. The density of each sample was calculated based on the sample mass and dimensions before exposure to heat. The mass and thickness of each sample were measured before and after each test to evaluate the surface recession and mass loss rate for each sample. Figure 8 shows the completed sample assembly before the arc heating test. Figure 9 shows the sample during the heating test.

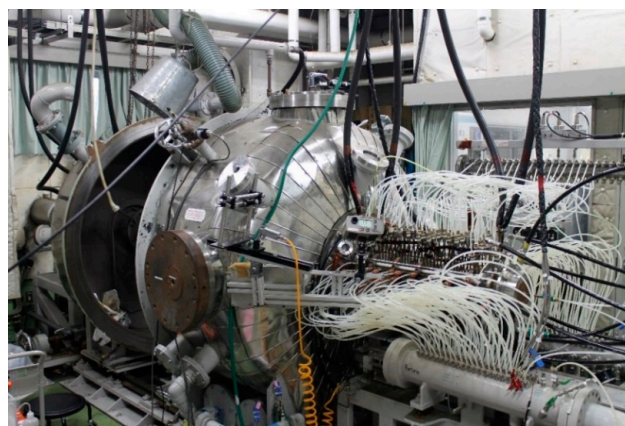


Figure 6. Arc heated wind tunnel facility located in JAXA ISAS.

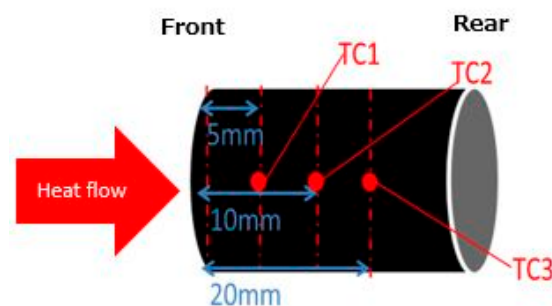


Figure 7. Location of thermocouples within sample including the direction of heat flow. TC refers to the thermocouple.

Table 7. Test conditions for arc heating test.

Group	Model	Environment	Density (kg/m ³) ¹	Heat Flux (MW/m ²)	Heating Duration (s)	Stagnation Pressure (kPa)
A	G1	Base sample	1395.3	5.0	20	12.46
	G2		1411.2	14.2	10	60.76
	H1		1359.2	5.0	20	12.46
	H2		1405.9	14.2	10	60.76
	A1		1412.2	5.0	20	12.46
	A2		1413.3	5.0	20	12.46
	A3		1415.4	5.0	20	12.46
	A4		1419.7	5.0	20	12.46
B	B1	2800 thermal cycles	1405.9	5.0	20	12.46
	B2	2800 thermal cycles	1414.4	5.0	20	12.46
	C1	4200 thermal cycles	1412.2	5.0	20	12.46
	C2	4200 thermal cycles	1411.7	5.0	20	12.46
	D1	5600 thermal cycles	1409.1	5.0	20	12.46
	D2	5600 thermal cycles	1412.2	5.0	20	12.46
	E1	15 ESD UV fluence	1409.1	5.0	20	12.46
	E2	15 ESD UV fluence	1413.3	5.0	20	12.46
	F1	30 ESD UV fluence	1410.6	5.0	20	12.46
	F2	30 ESD UV fluence	1410.6	5.0	20	12.46
	G1	45 ESD UV fluence	1411.2	5.0	20	12.46
	G2	45 ESD UV fluence	1419.7	5.0	20	12.46

¹ The mean (M) was 1408.60 kg/m³ with a standard deviation (SD) of 12.40.

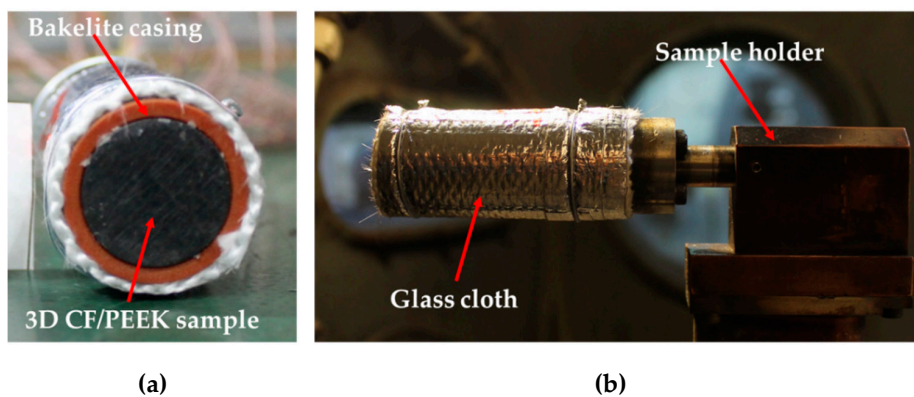


Figure 8. Completed sample wrapped in glass cloth and Bakelite attached to the sample holder: (a) front view of the sample; and (b) side view of the sample attached to the sample holder.

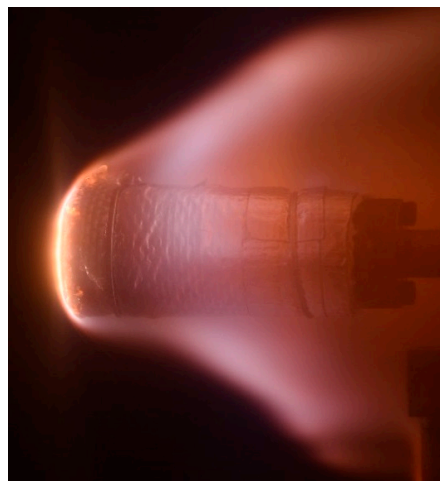


Figure 9. View of ablator sample inside the arc heating chamber during the test.

3. Results

This section summarizes the results of the tensile test and arc heating test for the 3D CF/PEEK ablator samples.

3.1. Tensile Test Results

During re-entry, the heatshield of a spacecraft must endure aerodynamic heating and loading. This section focuses on the area of aerodynamic loading. The 3D CF/PEEK serves both as an ablative heat shield and as a structural member of the TPS. The ablator material needs to have specific strength and specific rigidity [1]. Both of the mentioned properties are dependent on tensile strength and Young's modulus [24]. Figure 10 shows the effect of the different numbers of thermal cycles and UV fluence on the average tensile strength. The tensile strength of the samples decreased with an increase in the number of thermal cycles. The tensile strength decreased as much as 8.5% after 5600 thermal cycles as compared to the base sample. However, a different behavior was observed for samples exposed to UV radiation. There was an increase in tensile strength until 30 ESD before the tensile strength decrease. The increase was as much as 6.7% compared to the base sample.

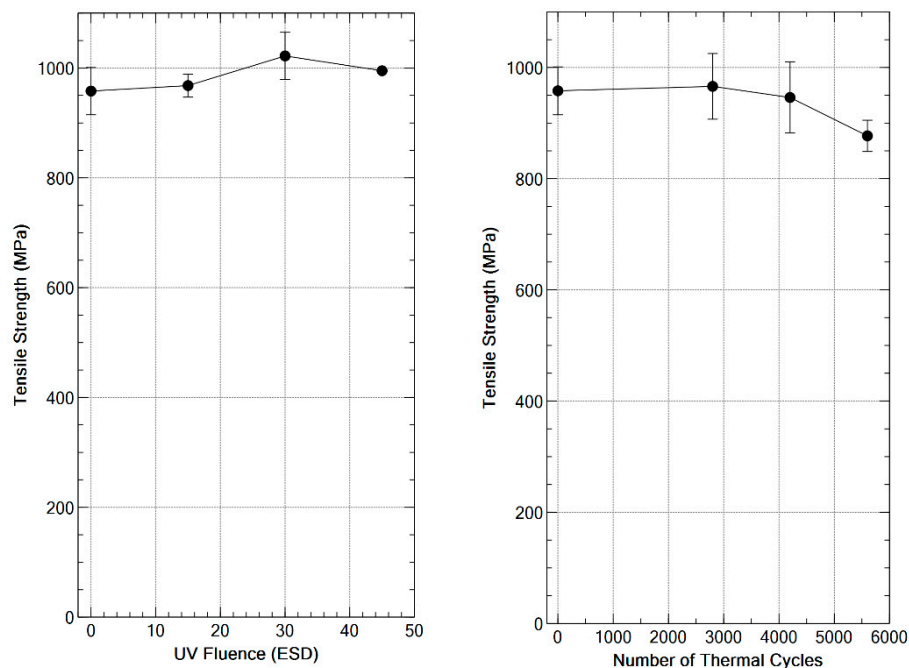


Figure 10. Effect of variation in the number of thermal cycles and UV fluence on the tensile strength of 3D CF/PEEK.

Figure 11 shows the effect of thermal cycles and UV fluence on Young's modulus. A decrease in average Young's modulus was also observed with an increase in the number of thermal cycles. The maximum decreased was 3.2% compared to the base sample. However, samples exposed to UV radiation experienced a small but gradual increase of 2.5% in the value of Young's modulus compared to the base sample. Overall, tensile strength incurred more changes compared to Young's modulus when exposed to the different numbers of thermal cycles and UV fluence.

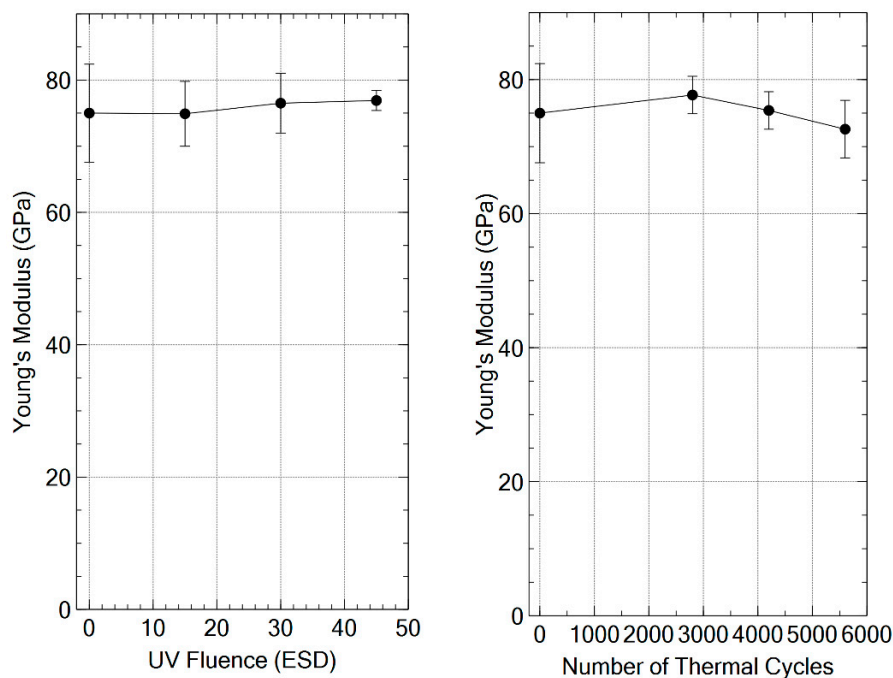


Figure 11. Effect of variation in the number of thermal cycles and UV fluence on the Young's Modulus of 3D CF/PEEK.

3.2. Surface Expansion Behavior

Figure 12 shows sample A1 before and after the heating test. The charred surface of the sample after the test can be seen in Figure 12b. The length of all samples increased after completion of the test. The length measurement was performed using a caliper. The average increase in length, which is denoted as negative surface recession, ranges between 0.60 and 1.80 mm for all samples, as shown in Figure 13. A comparison between base samples and thermally cycled showed a decrease in sample expansion as the number of thermal cycles increased. The same behavior was shown by samples irradiated with UV. The sample expansion decreased with an increase in UV fluence. However, the amount of decrease is less compared to samples exposed to thermal cycle conditions.

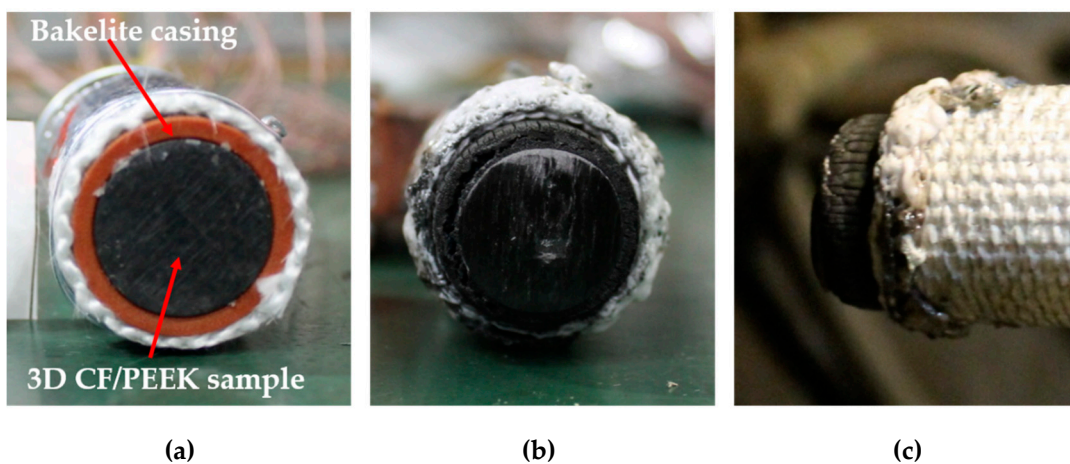


Figure 12. External view of ablator sample before and after arc heating test: (a) front view of sample before arc heating test; (b) front view of the sample after test; and (c) side view of the sample after the test.

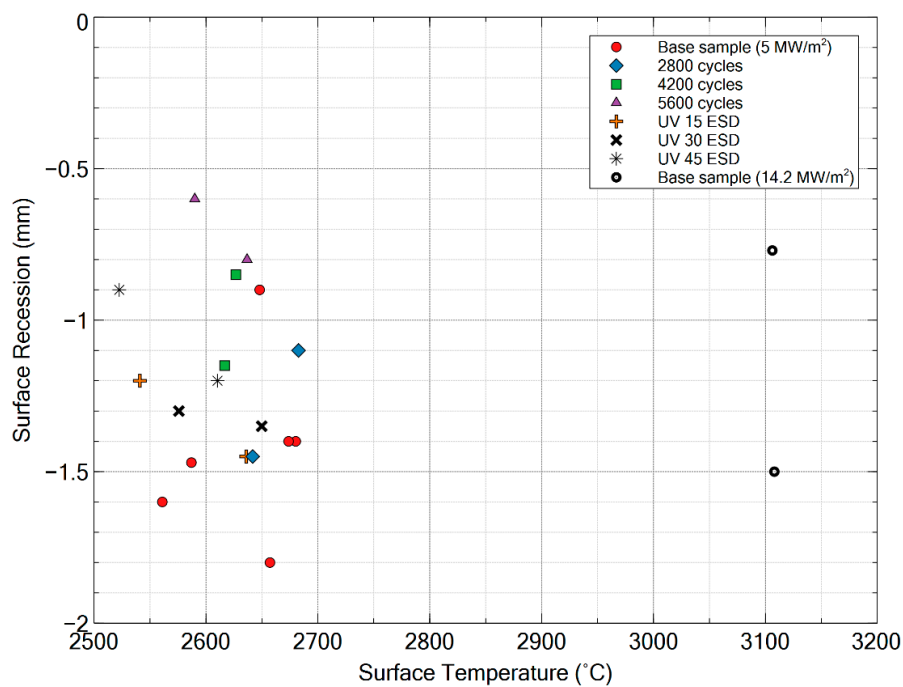


Figure 13. Relationship between surface recession with maximum surface temperature of 3D CF/PEEK.

3.3. Surface and Internal Temperature Behavior

Table 7 described the test conditions to observe the surface and internal temperature behavior. Figure 14 shows the relationship between heat flux and maximum surface temperature. The average maximum surface temperature increased from 2634.6 to 3107.1 °C when the heat flux increased from 5 to 14.2 MW/m². A comparison of the in-depth temperature–time histories between heat fluxes of 5 and 14.2 MW/m² is shown in Figure 15. The in-depth temperature for the sample exposed to 5 MW/m² heat flux is comparatively higher than the samples exposed to 14.2 MW/m². The reason for the higher in-depth temperature for lower heat flux compared to higher heat flux was due to heating duration, thermal conductivity and thermal capacity of the test material. The samples were exposed to 14.2 MW/m² for 10 s while the heating time was 20 s for 5 MW/m². As a result, the higher heat flux samples were not able to reach a higher temperature.

Figure 16 shows the time history of the surface temperature for base, thermally cycled and UV irradiated samples. Initially, there was a sharp increase in temperature, as shown in Figure 16a. The initial sharp increase happened when the ablator sample entered the plasma flow. As heating time increases, the change in surface temperature decreases and is nearly constant. The temperature then decreased back to the ambient temperature of the plasma due to the sample exiting the plasma jet. The same overall pattern can be observed in Figure 16b. The near-constant surface temperature might arise from the blocking action by pyrolysis gas. The product of the pyrolysis reaction in the PEEK resin produces gas that forms a protective layer from the hot stream over the char surface [25]. Moreover, when the surface temperature rises above 1500 K or 1230 °C, nearly all oxygen is consumed by the reaction at the surface. As a result, the reaction rate is limited, resulting in the near-constant surface temperature [26]. Table 8 shows the average maximum surface temperature for each ablator sample. Comparison in time history of surface temperature and maximum surface temperature showed no significant difference between base sample, thermally cycled and UV irradiated samples.

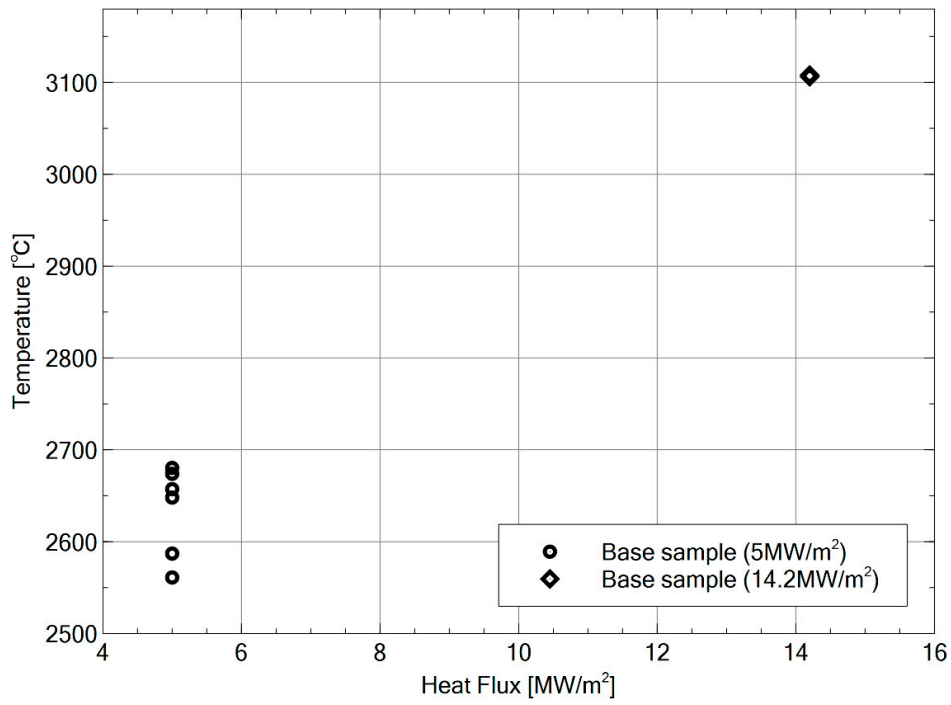


Figure 14. Relationship between maximum surface temperature and heat flux.

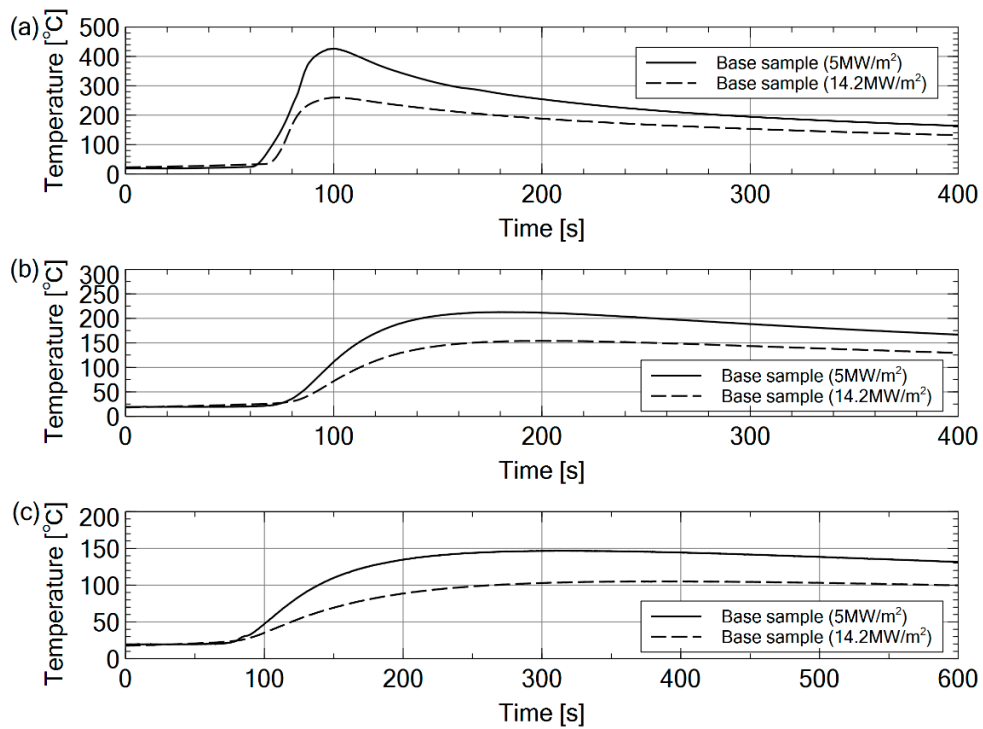


Figure 15. Comparison in time history of in-depth temperature between sample exposed to 5 and 14.2 MW/m²: (a) temperature at a depth of 5 mm; (b) temperature at a depth of 10 mm; and (c) temperature at a depth of 20 mm.

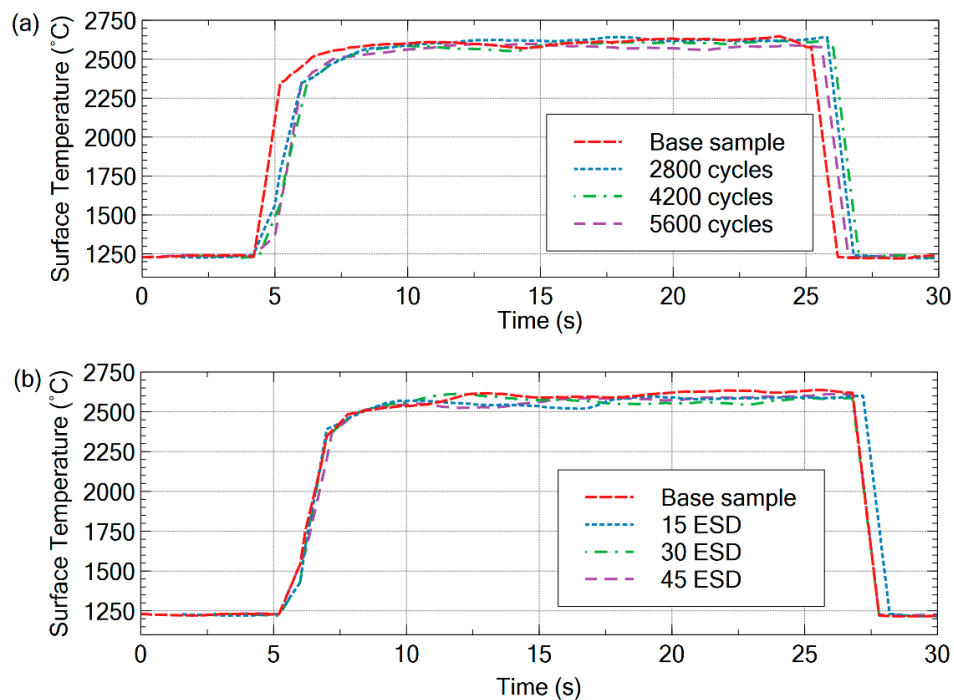


Figure 16. Time history of surface temperature during arc heating test: (a) comparison between the base sample and thermally cycled samples; and (b) comparison between the base sample and UV irradiated samples.

Table 8. The average maximum surface temperature for difference ablator samples during arc heating test.

Sample Type	Average Maximum Surface T (°C)
A (Base sample)	2640.78
B (2800 thermal cycles)	2662.25
C (4200 thermal cycles)	2621.75
D (5600 thermal cycles)	2613.38
E (15 ESD)	2588.48
F (30 ESD)	2612.83
G (45 ESD)	2566.44

Figure 17 shows the maximum temperature at different distances from the heated surface for all types of ablator samples. Thermocouples were located inside each sample at distances of approximately 5, 10 and 20 mm from the sample surface to measure inside temperature. The slight variation in thermocouple position for the same depth affected the maximum temperature. For the 5-mm reference point, the position of the thermocouples varied between 4.1 and 6.6 mm. The variation in position was due to error during the placement of thermocouple. Thermocouples with location of 4.1 and 4.2 mm recorded higher temperatures between 650 and 1050 °C. Most of the recorded temperatures were within 300–500 °C for the 5-mm distance, as shown in Figure 17a. The plot for the maximum temperature as a function of distance from the surface is not linear but a gradual downward curve. The temperature was approximately 250 °C at 10 mm before reaching 150 °C at 20 mm from the surface.

There was a small difference in maximum temperature between different sample types near the surface, as shown in Figure 17a. The temperature difference gradually diminishes for 10- and 20-mm distance from the surface. Figure 17b shows a detailed internal temperature around the 5-mm reference point. Thermally cycled samples show a slightly higher maximum temperature compared to the base samples between 4.5 and 6 mm.

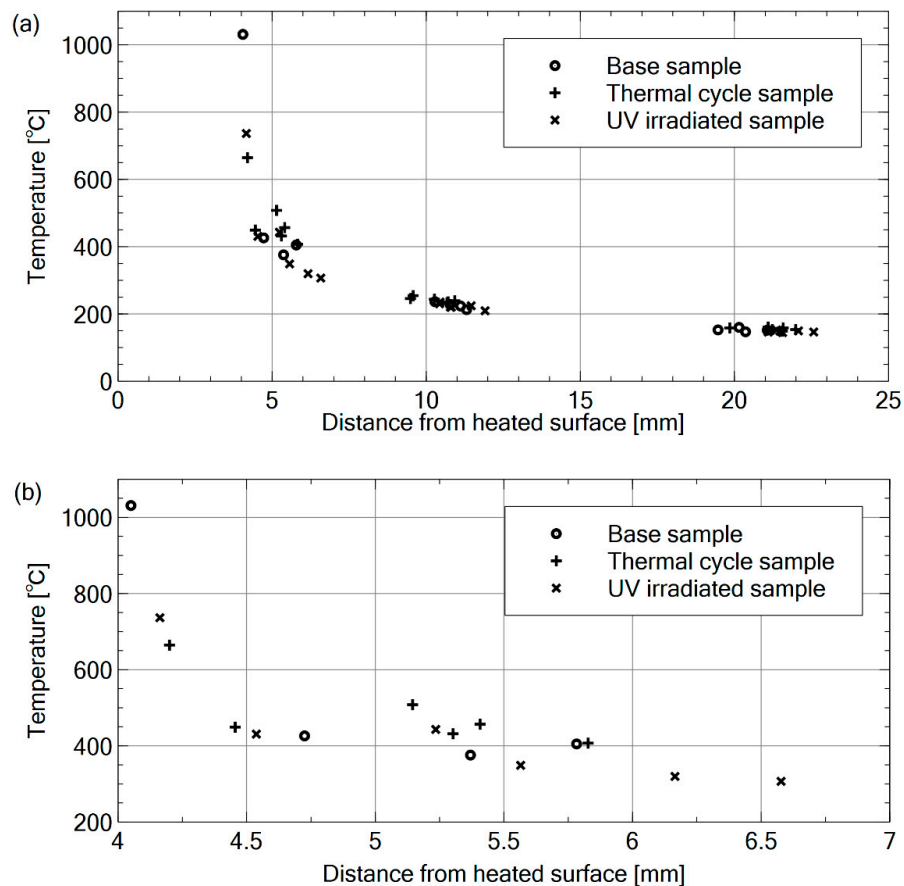


Figure 17. Comparison of the maximum temperature at different depths for all types of 3D CF/PEEK samples: (a) overall internal maximum temperature; and (b) detailed internal maximum temperature near 5-mm reference point.

3.4. Recession Behavior

Two parameters were considered in analyzing the recession behavior of the 3D CF/PEEK ablator. The parameters were as follows:

1. Surface recession.
2. Mass loss rate.

The following sections discuss the effect of the thermal cycle, UV radiation and different heat flux on the two mentioned parameters.

3.4.1. Surface Recession Rate

Figure 18 shows the relationship between surface recession rate and maximum surface temperature for all samples. The surface recession was obtained using Equation (3) [1].

$$\dot{L} = \frac{L}{t} \quad (3)$$

where \dot{L} is the surface recession rate (m/s), L is the amount of surface recession (m) which is the length or thickness of the sample before and after heating and t is the heating duration (s). Negative values were observed for the surface recession rate of all samples. The negative values implied that the surface expanded instead of decreased, as discussed in Section 3.2. Surface recession ranges between -0.00003 and -0.00015 m/s. The surface recession rate decreased with an increase in surface temperature due to increased heat flux. In other words, the surface expansion rate increased with increased surface

temperature. The surface recession rate for the thermally cycled sample and UV irradiated sample vary near the base sample with an increase in surface temperature.

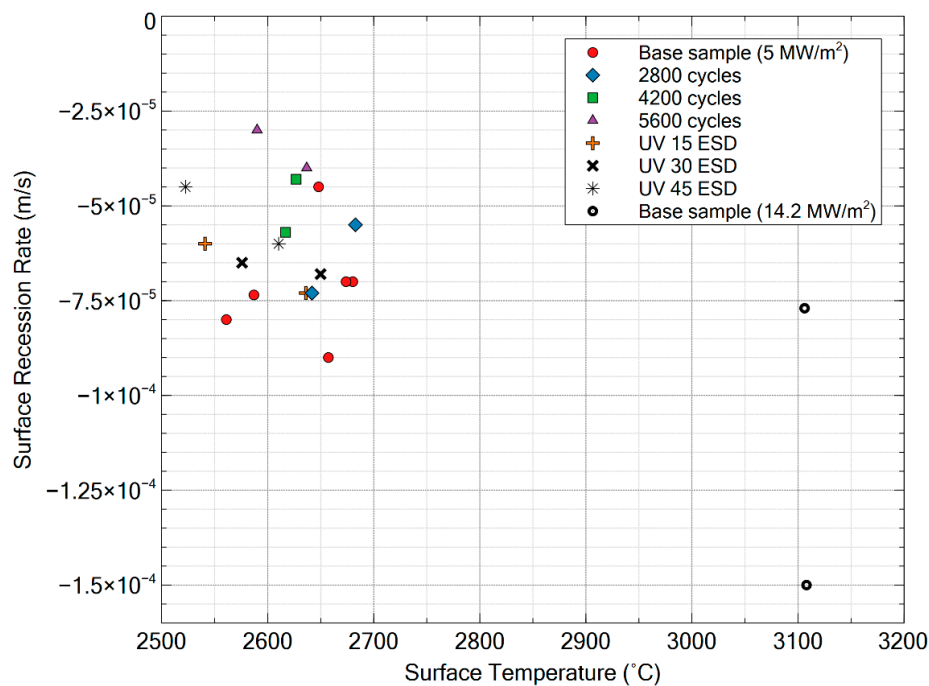


Figure 18. The relationship between maximum surface temperature and surface recession rate of 3D CF/PEEK.

Table 9 shows the average surface recession for different 3D CF/PEEK samples. The base sample has the lowest surface recession rate while the thermally cycled sample has the highest surface recession rate. A gradual increase in surface recession rate can be observed with an increase in the number of thermal cycles. The surface recession rate was near-constant with a small increase in samples irradiated with 45 ESD. The mentioned results imply a marginally lower surface expansion rate for thermally cycled samples compared to base samples. However, the surface expansion rate for UV radiated samples was almost identical to base samples. Based on the previous observations, it can be concluded that the thermal cycle and UV radiation have a minor impact on the surface recession rate properties of 3D CF/PEEK ablator in LEO.

Table 9. The average surface recession for difference ablator samples after arc heating test.

Sample Type	Average Surface Recession Rate (m/s)
A (Base sample)	-0.000071
B (2800 thermal cycles)	-0.000064
C (4200 thermal cycles)	-0.000050
D (5600 thermal cycles)	-0.000035
E (15 ESD)	-0.000066
F (30 ESD)	-0.000066
G (45 ESD)	-0.000052

3.4.2. Mass Loss Rate

The degradation mode during ablation depends on the surface temperature [27]. Figure 16 shows that surface temperature was predominantly around 2600 °C for the 5 MW/m² heat flux. Coupled with a modest heating rate of 5 MW/m², the surface ablation was by the diffusion-controlled oxidation mode. The mass-loss rate in diffusion-controlled oxidation mode is governed by Equation (4) [1].

$$\dot{m}_D = C_0 \sqrt{P_e/R_B} \quad (4)$$

where \dot{m}_D is the mass loss rate ($\text{kg}/\text{m}^2/\text{s}$), C_0 is the diffusion-controlled mass-transfer constant ($\text{kg}/\text{m}^{3/2} \cdot \text{s} \cdot \text{Pa}^{1/2}$), P_e is the stagnation pressure (Pa) and R_B is the radius of the sample (m). The front of the sample is flat instead of hemispherical. Therefore, the value of R_B is obtained by multiplying the sample diameter by 2.463. The mass-loss rate can also be calculated based on measured data using Equation (5).

$$\dot{m} = \frac{m_f - m_i}{A \cdot t} \quad (5)$$

where \dot{m} is the mass loss rate ($\text{kg}/\text{m}^2/\text{s}$), m_f is the sample mass after heating (kg), m_i is the initial sample mass before heating (kg), t is the heating duration (s) and A is the frontal area of the sample (m^2). In this experiment, the frontal area of the sample is equivalent to the area of a circle. Figure 19 shows the mass-loss rate to surface temperature for all samples. Mass loss rate increased with an increase in surface temperature due to an increase in heat flux. Samples exposed to 45 ESD of UV radiation showed the highest difference in mass loss rate compared to base samples. The other samples showed a mass loss rate ranging between 0.095 and 0.12 $\text{kg}/\text{m}^2/\text{s}$. There is no significant difference between all samples except for the samples exposed to higher heat flux.

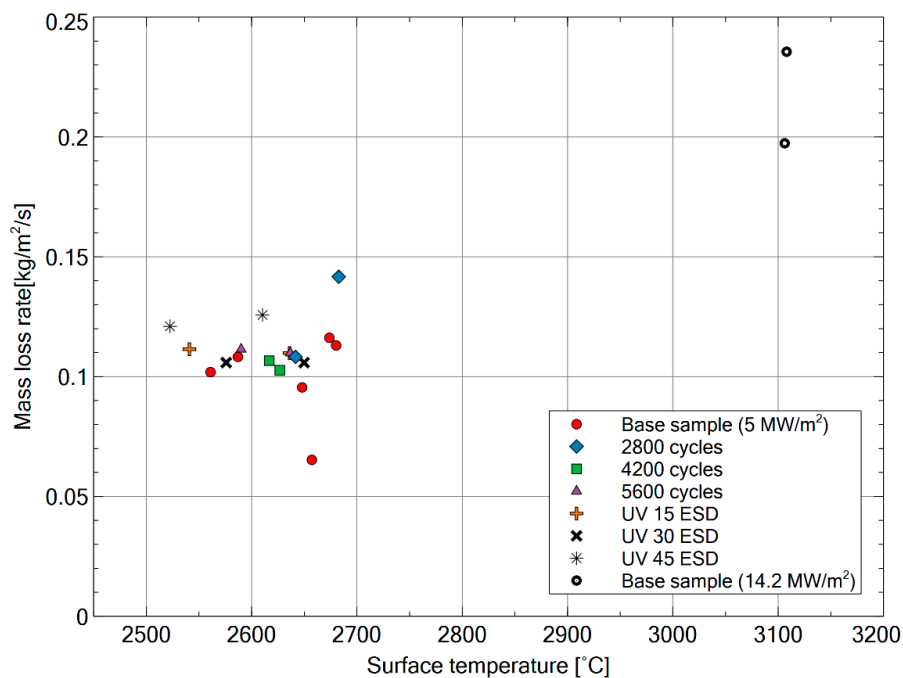


Figure 19. The relationship between mass-loss rate and maximum surface temperature of 3D CF/PEEK.

4. Discussion

4.1. Changes in Mechanical Properties

In the space environment, the temperature can vary between -160 and $+120$ °C when a satellite passes from direct sunlight into Earth shadow [9]. This process repeats continuously throughout the satellite mission life and is termed as thermal cycling. Figure 10 shows that there is a small decrease in tensile strength after 5600 thermal cycles. However, Young's modulus did not change significantly after 5600 thermal cycles. This trend occurred because the thermal cycle can have limited degradation effect on tensile strength and Young's modulus. The thermal cycle primarily affects matrix dominated properties such as compression and coefficient of thermal expansion (CTE) [17,28]. Tensile strength and Young's modulus are dominated by the fiber properties, thus are not severely affected by the

thermal cycle [29]. The results for the thermally cycled samples were consistent with previous studies whereby 500 thermal cycles from approximately -150 to $+93$ °C did not significantly change tensile strength and Young's modulus for CF/PEEK composites [10].

About UV radiation, both chain scission and crosslinking can affect the PEEK resin [14]. Chain scission creates weak bonds in polymers by cutting molecular chains. Crosslinking caused embrittlement of the polymer by limiting the movement of the molecular chain [30]. An increase in UV exposure duration can increase the crystallinity of the polymer [31]. Crystallization leads to tighter packing of the polymer chains thus resulting in stronger intermolecular bonding forces between the chains [32]. An increase in the percentage of crystallinity can improve the tensile properties of polymers in composites. Hence, as shown in Figure 10, the tensile strength initially increases until the point of 30 ESD. The initial increase in tensile strength suggests the increase in the crystallization of PEEK. The tensile strength subsequently decreases after 30 ESD. After 30 ESD the degradation by chain scission is more dominant than the crystallization of PEEK resulting in the decrease of tensile strength. However, further investigation should be devoted to determining the percent crystallinity at various UV fluence. However, Figure 11 shows an increasing Young's modulus but at a decreasing rate as the UV fluence increases to 45 ESD. The increasing trend in Young's modulus suggests that PEEK became embrittled due to crosslinking. Moreover, the increased crystallinity due to the longer duration to UV can increase Young's modulus [31,33].

4.2. Recession Behavior

Increase in the length of sample or surface expansion was observed in all 3D CF/PEEK samples after the arc heating test. Previous tests using traditional CF/PEEK that was not 3D printed, hereafter referred to as CF/PEEK, showed the same behavior. In contrast, previous tests involving Lightweight Ablator Series for Transfer Vehicle System (LATS) ablator showed surface recession or decreased in the length of ablator samples [34]. LATS is a lightweight CFRP ablator material made of carbon fiber impregnated with phenolic resin [35]. A lightweight ablator based on LATS was used in the recently recovered H-II transfer vehicle (HTV) small re-entry capsule on November 27, 2018 [36]. A comparison between the surface recession between 3D CF/PEEK, CF/PEEK and LATS ablator materials is shown in Figure 20. The surface expansion is represented by a negative surface recession in Figure 20.

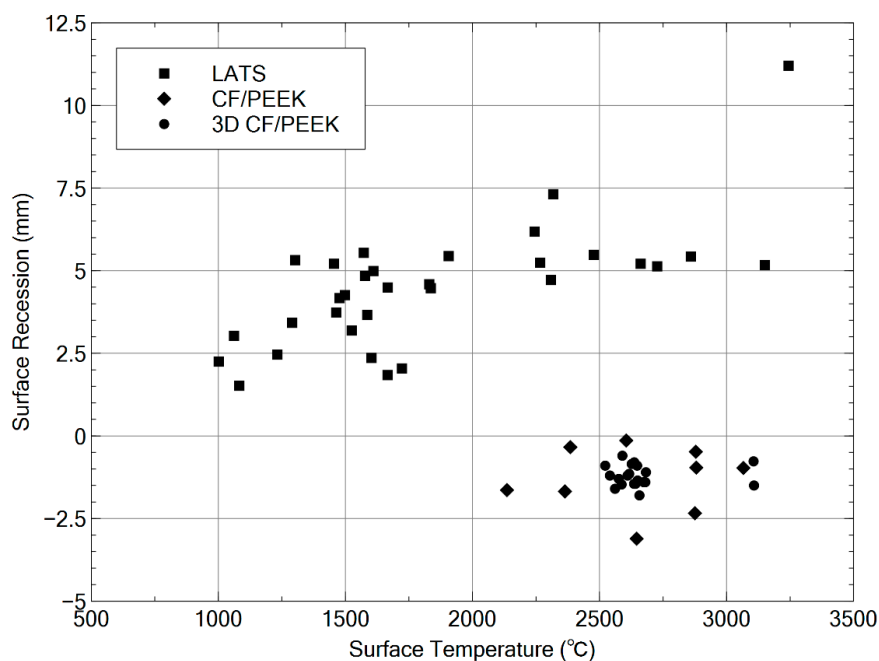


Figure 20. Comparison of surface recession between 3D CF/PEEK, CF/PEEK and LATS. The negative surface recession denotes a surface expansion.

A comparison of surface recession rate also showed the same behavior as the surface recession, as shown in Figure 21. The surface recession rate for 3D CF/PEEK and CF/PEEK shows a negative value, implying that the surface expanded. However, the surface recession rate for LATS showed a positive value due to surface recession.

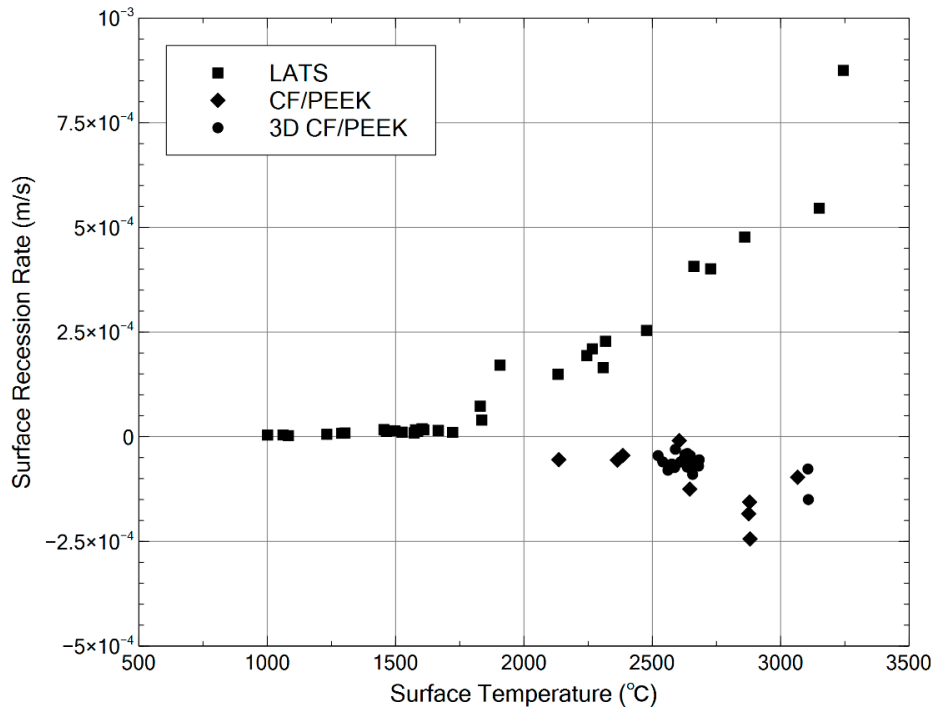


Figure 21. Comparison of surface recession rate between 3D CF/PEEK, CF/PEEK and LATS. The negative surface recession rate denotes a surface expansion rate.

Various processes happened during the ablation of a heat shield as discussed in Introduction. The primary recession mechanism is through the thermochemical process [37]. However, the process of delamination also occurred during the ablation of 3D CF/PEEK in addition to the thermochemical reaction. Figure 22 shows the side view of the base, thermally cycled and UV irradiated samples after arc heating test. The pyrolysis reaction of the PEEK resin released pyrolysis gas which creates pressure in the out-of-plane direction inside the sample structure. Delamination occurs when the pressure due to the pyrolysis gas exceeds the interlaminar strength. In a previous study, pressure from pyrolysis gas was identified as the cause of delamination in CFRP ablators [38]. Therefore, during the ablation of 3D CF/PEEK, the thermochemical process caused surface recession while the delamination and material expansion cause surface expansion. Note that the recession process is dependent on the surface temperature whereby the surface recession and expansion rate increase with an increase in surface temperature as shown in Figure 21.

Therefore, it is suspected that the surface recession rate is less than the surface expansion rate, resulting in surface expansion being the dominant process during the ablation of 3D CF/PEEK. As a result, the surface of 3D CF/PEEK samples expanded, as shown in Figure 20. The lower surface recession rate is due to the higher activation energy (E) of 3D CF/PEEK compared to CFRP used in LATS.

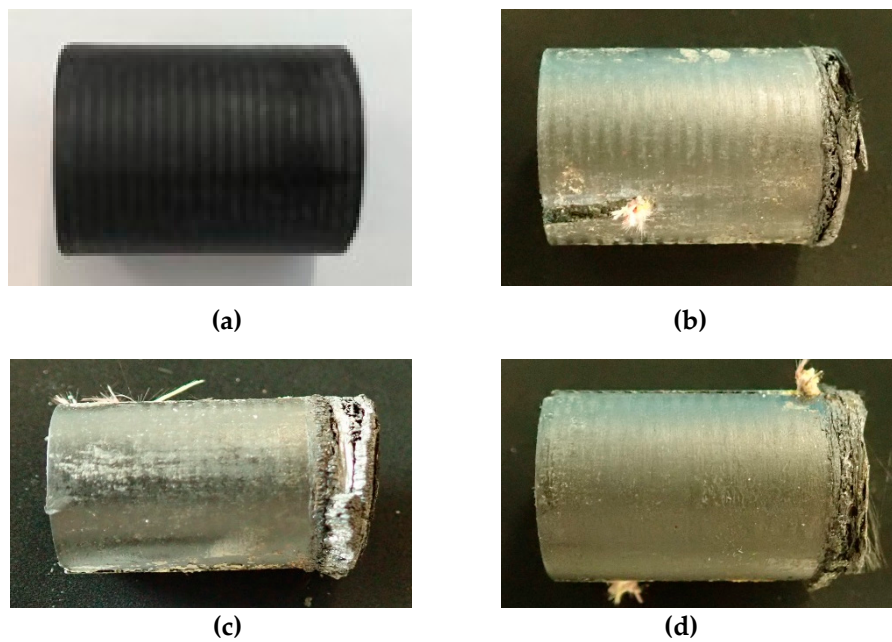


Figure 22. Side view of ablator sample used in arc heating test: (a) base sample before the test; (b) base sample after test; (c) thermally cycled sample; and (d) UV irradiated sample.

Activation energy can be calculated using Equation (6) [4]. The same equation is used to calculate the mass-loss rate, \dot{m}_R (kg/m²/s), in the rate-controlled oxidation region [4].

$$\dot{m}_R = k_0 \sqrt{X_0 P_e} e^{-E/RT_W} \quad (6)$$

where \dot{m}_R is the mass loss rate (kg/m²/s), k_0 is collision frequency (kg/s·m²·Pa^{1/2}), X_0 is the mole fraction of oxygen in the air (0.21), P_e is the stagnation pressure (Pa), E is the activation energy (J/mol), R is the universal gas constant (8.318 J/mol/K) and T_W is wall temperature (K). Taking the logarithm of both sides resulted in Equation (7) [4].

$$\ln(\dot{m}_R) = -\frac{E}{RT_W} + \ln(k_0 \sqrt{X_0 P_e}) \quad (7)$$

Figure 23 shows the relationship between the logarithmic mass loss rate and the reciprocal of the surface temperature for all types of samples. Based on Figure 23, the slope or E/R for 3D CF/PEEK is 15,319 K. The slope value was multiplied with the R -value to obtain the activation energy of 127.4 kJ/mol. The E value for 3D CF/PEEK is about 10% more compared to 115.6 kJ/mol of CF/PEEK. However, the E value is much higher compared to the CFRP ablator using phenolic resin which is 83.3 kJ/mol [39]. Therefore, the higher E value for 3D CF/PEEK compared to CFRP ablators caused the lower surface recession rate. The minor difference between activation energy of 3D CF/PEEK and CF/PEEK is due to the resin content. The activation energy is dependent on resin content [1]. The CF/PEEK used in the previous heating test has a resin content of 63% compared to 44% for the 3D CF/PEEK. The collision frequency is then calculated by substituting the surface mass loss rate of 3D CF/PEEK, the material surface temperature, the stagnation pressure measured during test and the activation energy of 3D CF/PEEK into Equation (6). The average collision frequency based on measured experimental values was 0.331 kg/s·m²·Pa^{1/2}.

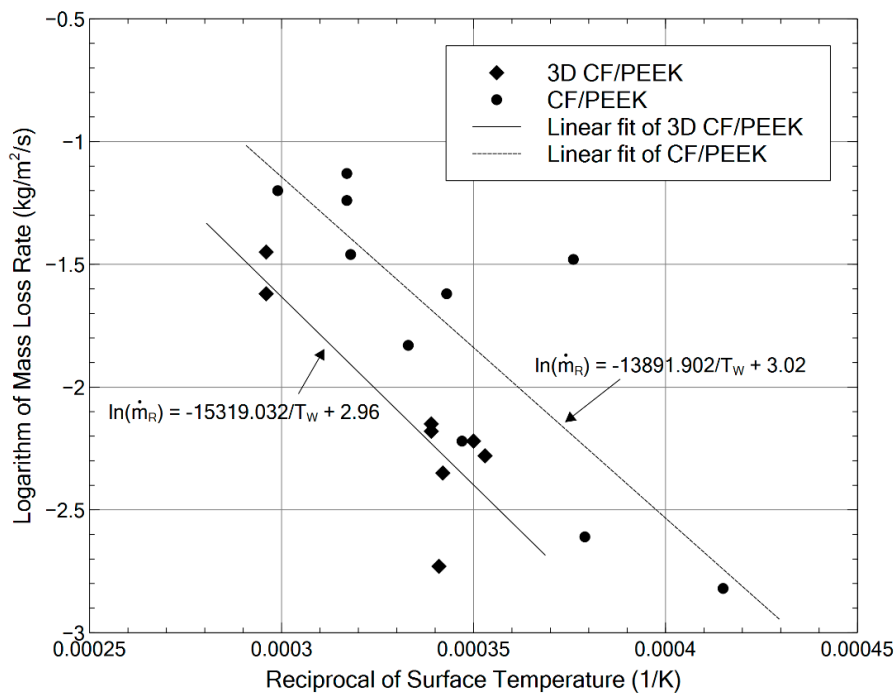


Figure 23. The relationship between reciprocal of surface temperature and the logarithm of mass loss rate of 3D CF/PEEK and CF/PEEK.

Based on the mass-loss rate calculated using Equation (5), the C_0 was obtained using the linear relationship between $\sqrt{P_e/R_B}$ and the mass loss rate shown in Equation (4) [39]. The C_0 value affects the maximum value of the mass-loss rate. Figure 24 shows the relationship between the mass-loss rate of 3D CF/PEEK and $\sqrt{P_e/R_B}$ based on measured data. The slope in Figure 24 or C_0 value of 3D CF/PEEK is $1.996 \times 10^{-4} (kg/m^{3/2} \cdot s \cdot Pa^{1/2})$, which is lower than the C_0 value for CF/PEEK. An increase in C_0 meant an increase in the mass loss rate [1]. Therefore, 3D CF/PEEK has a lower mass-loss rate compared to CF/PEEK.

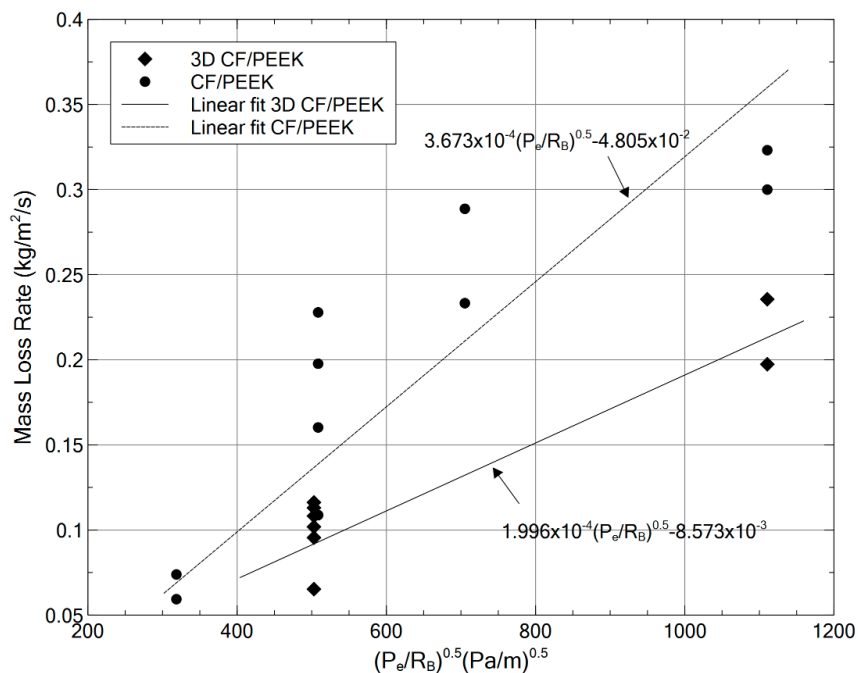


Figure 24. The relationship between the mass-loss rate and $\sqrt{P_e/R_B}$ of 3D CF/PEEK and CF/PEEK.

Figure 25 shows a comparison in the relationship between mass-loss rate and maximum surface temperature for 3D CF/PEEK, CF/PEEK and LATS. Based on Figure 25, 3D CF/PEEK has the lowest mass loss rate comparative to CF/PEEK and LATS. The lower mass-loss rate of 3D CF/PEEK can be attributed to the higher activation energy compared to LATS and CF/PEEK. The small difference in mass loss rate between 3D CF/PEEK and CF/PEEK is attributed to higher activation energy and lower C_0 value in 3D CF/PEEK compared to CF/PEEK. In conclusion, the higher activation energy caused 3D CF/PEEK to be less susceptible to surface recession and mass loss but more affected by surface expansion due to delamination and thermal expansion.

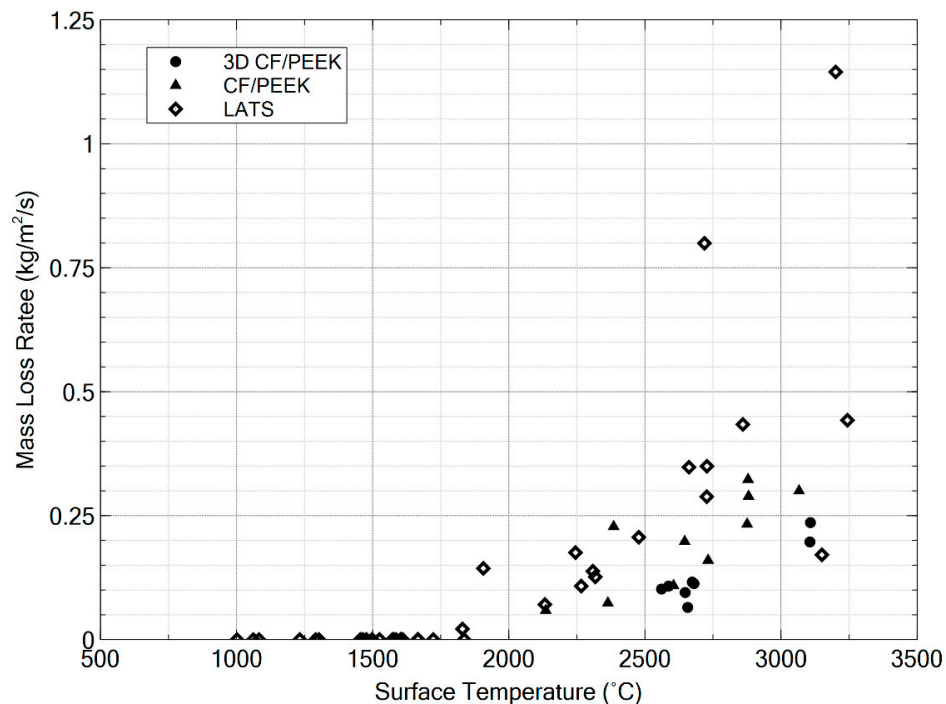


Figure 25. The relationship between mass-loss rate and mass loss rate of 3D CF/PEEK, CF/PEEK and LATS.

Figure 13 shows that an increase in the amount of thermal cycle caused the amount of surface expansion to be decreased. Samples exposed to 5600 thermal cycles, equivalent to one year, showed a marginally lower surface expansion rate compared to base samples. Thermal cycles can affect the CTE of a sample due to the advent of microcracks within the sample structure. It is suspected that the CTE value decreases when the number of thermal cycles increased. The reason is that the damage to the matrix by microcracking caused the CTE to be dominated by the fiber, thus decreasing the CTE value. Studies have shown that fiber has a lower CTE compared to the matrix [40]. Moreover, another study showed that pores at the interface between consequently deposited layers in a 3D printed CF/PEEK can lead to multiple crack formation. The cracks can affect the CTE value compared to CF/PEEK [41]. Therefore, it is suspected that the decrease in CTE value restricts the surface from expanding thus decreasing the surface expansion rate.

4.3. Surface and Internal Temperature Behavior

Figure 26 shows the variation in maximum surface temperature with heat flux for different ablator materials. The results for 3D CF/PEEK whereby surface temperature increases with an increase in heat flux is consistent with previous tests involving LATS and CF/PEEK. Figure 17 shows that maximum temperature as a function of distance from the surface is not linear but a gradual downward curve. The nature of the curve plot is due to the dependence of the thermal conductivity of ablator material on the density of resin [1]. The thermal decomposition of resin near the surface during the arc heating

test resulted in a charred surface. The porous charred surface and near-surface area are less dense than the virgin material inside the ablator [42]. As a result, the thermal conductivity decreases due to the porosity and decrease in density [43]. Based on Figure 16, the maximum surface temperature was on average approximately 2600 °C. The temperature then sharply decreased to 500 °C at 5 mm from the surface. The sharp drop can be explained by the porous region near the surface area which has low thermal conductivity.

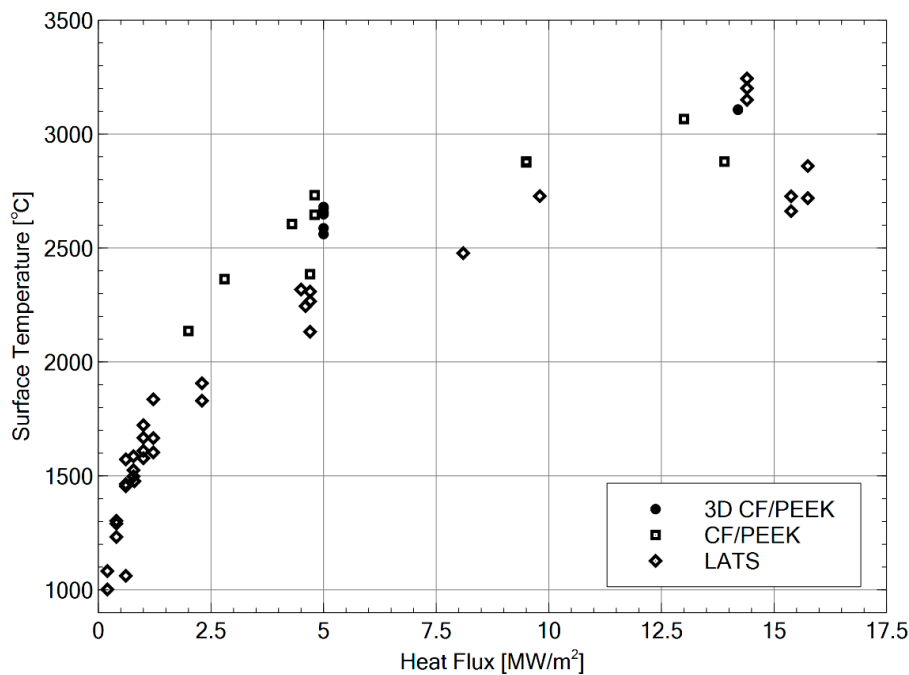


Figure 26. The relationship between maximum surface temperature and heat flux for different ablator materials.

A comparison of in-depth temperature between different sample types shows a slightly higher trend in temperature for thermally cycled samples. The difference is mainly in the region between 4.5 and 6 mm, as shown in Figure 17. The primary effect of thermal cycling is to induce microcracks inside the structure of a material [7]. Previous studies have shown that the orientation of a crack can affect the thermal conductivity of a material [43,44]. It is suspected that microcracks in the near-surface area affect the thermal conductivity property of the ablator material. However, the magnitude of the difference in temperature value between thermally cycled samples and base samples is not significantly large. Therefore, exposure to the thermal cycle has no significant effect on the internal temperature behavior of ablator samples.

Figure 27 shows that the surface temperatures of 3D CF/PEEK, CF/PEEK and LATS were nearly identical when exposed to a heat flux of approximately 5.0 MW/m². The in-depth temperature for 3D CF/PEEK is almost identical to CF/PEEK and lower than LATS at 20 mm from the surface.

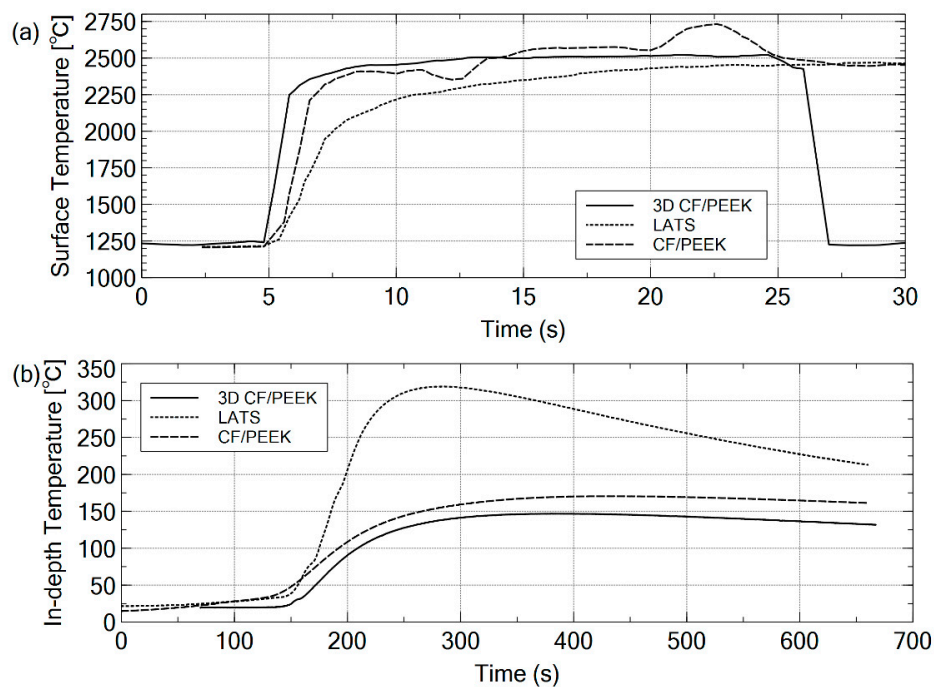


Figure 27. Comparison of maximum surface and in-depth temperature between 3D CF/PEEK, LATS and CF/PEEK ablator samples: (a) maximum surface temperature; and (b) maximum in-depth temperature for 20 mm from surface.

4.4. Future Works

Previously discussed results concerning the effect of thermal cycle and UV radiation were limited to surface recession rate, surface temperature and in-depth temperature behavior. The next step will be to determine the effect of the thermal cycle and UV radiation on the activation energy and diffusion-controlled mass-transfer constant. Both parameters can affect the surface recession rate and mass loss rate [1]. Arc heating test conducted in a wider range of heat flux and heating duration using thermally cycled and UV irradiated samples can facilitate study on the effects of thermal cycle and UV radiation on the mentioned parameters.

Accurate prediction of the recession and temperature behavior of 3D CF/PEEK material during the re-entry environment is necessary for the design of the TPS. Previously, various ablation analysis codes, mainly one-dimensional ablation simulation codes, were developed to cater for high density and low-density CFRP-based ablator materials [3,45]. However, the suitability of the existing ablation codes has not yet been confirmed for 3D CF/PEEK. To improve the existing codes, the following may prove to be useful:

1. Execution of further arc heating test using different heat flux and heating duration, which among others can confirm the surface expansion behavior in different heating environments.
2. Determination of the density relation between virgin layer and char layer of 3D CF/PEEK.
3. Measurement of thermal conductivity and specific heat variation of 3D CF/PEEK with temperature.

5. Conclusions

In this research, a new heat shield material made of 3D printed CF/PEEK was evaluated using tensile and arc heating test. Young's modulus did not significantly change after exposure to an increasing number of thermal cycles and UV fluence. However, tensile strength showed a small decrease after exposure to the thermal cycle but no significant change after exposure to UV radiation. The length of the samples increased or the surface expanded during the heating test, resulting in a negative surface recession rate. The increased surface temperature increased the mass-loss rate.

The surface expansion rate was more than the surface recession rate for 3D CF/PEEK resulting in an expanded surface. The lower surface recession rate was due to a higher activation energy for 3D CF/PEEK compared to CFRP based ablator such as LATS. The activation energy for 3D CF/PEEK was marginally higher than CF/PEEK due to difference in resin content. Moreover, 3D CF/PEEK has the lowest mass loss rate compared to LATS and CF/PEEK attributed to a higher activation energy. Therefore, 3D CF/PEEK high activation energy makes it less susceptible to surface recession and mass loss but more affected by surface expansion due to delamination and material expansion. The surface expansion decreased when the number of thermal cycles increased. Moreover, the surface expansion rate for samples exposed to the thermal cycle was marginally lower than other samples. It is suspected that a decrease in CTE value due to microcracks restricts surface expansion, thus decreasing surface expansion rate. However, the mass-loss rate was almost identical for base samples and samples exposed to the thermal cycle and UV radiation. The increased surface temperature of 3D CF/PEEK due to increasing heat flux was consistent with LATS and CF/PEEK. Exposure to similar heat flux yielded almost identical surface temperatures among 3D CF/PEEK, CF/PEEK and LATS. In-depth temperature for 3D CF/PEEK was almost identical to CF/PEEK but lower than LATS when exposed to similar heat flux. Samples exposed to the thermal cycle exhibited a marginally higher temperature in the near-surface region compared to other samples. However, the temperature difference between base samples and samples exposed to the thermal cycle and UV radiation gradually diminishes with an increase in depth. Overall, the thermal cycle and UV radiation have no significant effect on the surface and in-depth temperature behavior of samples. The new 3D CF/PEEK material has demonstrated excellent recession resistance while maintaining mechanical properties when exposed to high temperature, thermal cycle and UV radiation. Consequently, 3D CF/PEEK can be considered as a viable heat shield material for the re-entry flight.

Author Contributions: Conceptualization, F.A., A.M. and N.Y.; methodology, F.A., A.M., N.Y. and K.-i.O.; validation, F.A., N.Y. and K.-i.O.; formal analysis, F.A., A.M. and N.Y.; investigation, F.A., A.M. and N.Y.; resources, F.A., A.M., N.Y. and K.-i.O.; data curation, F.A., A.M. and N.Y.; writing—original draft preparation, F.A.; writing—review and editing, F.A. and K.-i.O.; visualization, F.A. and N.Y.; supervision, K.-i.O.; project administration, K.-i.O.; and funding acquisition, K.-i.O. All authors have read and agreed to the published version of the manuscript.

Funding: This research received no external funding.

Acknowledgments: This research was performed in collaboration with AGC Inc. This study could not be completed without the effort and co-operation from the Okuyama Lab team members.

Conflicts of Interest: The authors declare no conflict of interest. The funders had no role in the design of the study; in the collection, analyses, or interpretation of data; in the writing of the manuscript, or in the decision to publish the results.

Abbreviations

The following abbreviations were used in this manuscript:

AM	Additive Manufacturing
CAD	Computer-Aided Drawing
CF	Carbon Fiber
CFRP	Carbon Fiber Reinforced Plastic
CFRTP	Carbon Fiber Reinforced Thermoplastic
CTE	Coefficient of Thermal Expansion
DED	Direct Energy Deposition
ESD	Equivalent Solar Day
FDM	Fused Deposition Modelling
HTV	H-II Transfer Vehicle
ISAS	Institute of Space and Aeronautical Science
ISS	International Space Station
JAXA	Japan Aerospace Exploration Agency

LATS	Lightweight Ablator Series for Transfer Vehicle System
LEO	Low Earth Orbit
NASA	National Aeronautics and Space Administration
PBF	Powder Bed Fusion
PEEK	Polyether Ether Ketone
SLA	Stereolithography
SLS	Selective Laser Sintering
TPS	Thermal Protection System
UV	Ultraviolet
VUV	Vacuum Ultraviolet

References

- Okuyama, K.; Zako, M. A Study on Recession Characteristics of Completely Carbonized CFRP. *SPACE Technol. Jpn. Jpn. Soc. Aeronaut. SPACE Sci.* **2004**, *3*, 35–43. [CrossRef]
- Beck, R.A.S. *Ablative Thermal Protection Systems Fundamentals*; Thermal and Fluids Analysis Workshop: Huntsville, AL, USA, 2017.
- Kato, S.; Okuyama, K.; Gibo, K.; Miyagi, T.; Suzuki, T.; Fujita, K.; Sakai, T.; Nishio, S.; Watanabe, A. Thermal Response Simulation of Ultra Light Weight Phenolic Carbon Ablator by the Use of the Ablation Analysis Code. *Trans. Jpn. Soc. Aeronaut. SPACE Sci. Aerosp. Technol. Jpn.* **2012**, *10*, 31–39. [CrossRef]
- Metzger, J.W.; Engel, M.J. Oxidation and Sublimation of Graphite in Simulated Re-Entry Environments. *AIAA J.* **1967**, *5*, 10. [CrossRef]
- Hacopian, E.; Bouslog, S. *Technical Challenges with 3D Printing Heat Shields*; Advanced Manufacturing & Carbon Materials Workshop: Houston, TX, USA, 2018.
- ESA. 3D printing Cubesat bodies for cheaper, faster missions. Available online: http://www.esa.int/Enabling_Support/Space_Engineering_Technology/3D_printing_CubeSat_bodies_for_cheaper_faster_missions (accessed on 20 June 2020).
- Di Roberto, R. TUPOD. Available online: <https://www.gaussteam.com/satellites/gauss-latest-satellites/tupod/> (accessed on 4 April 2020).
- Bouslog, S. *3D Printing Heat Shields*; Additive Manufacturing & Advanced Materials Workshop: Houston, TX, USA, 2017.
- Cogswell, F.N. *Thermoplastic Aromatic Polymer Composites*; Butterworth-Heinemann: Oxford, UK, 1992; ISBN 978-0-7506-1086-5.
- Funk, J.G.; Sykes, G.F. *The Effects of Simulated Space Environmental Parameters on Six Commercially Available Composite Materials*; National Aeronautics and Space Administration: Hampton, VA, USA, 1989; p. 34.
- Slemp, S. *Ultraviolet Radiation Effects*; NASA, Scientific and Technical Information Office: Hampton, VA, USA, 1989; p. 22.
- Tennyson, R.C. Atomic Oxygen and Its Effect on Materials. In *The Behavior of Systems in the Space Environment*; DeWitt, R.N., Duston, D., Hyder, A.K., Eds.; Springer Netherlands: Dordrecht, The Netherlands, 1993; pp. 233–257. ISBN 978-94-010-4907-8.
- Johnson, R.H.; Montierth, L.D.; Dennison, J.R.; Dyer, J.S.; Lindstrom, E.R. Small-Scale Simulation Chamber for Space Environment Survivability Testing. *IEEE Trans. Plasma Sci.* **2013**, *41*, 3453–3458. [CrossRef]
- Nakamura, T.; Fujita, O. Effects of LEO Environment on Mechanical Properties of Peek Films under Tensile Stress. In Proceedings of the Proc. of International Symposium on “SM/MPAC&SEED Experiment”, Tsukuba, Japan, 10–11 March 2008; p. 8.
- Zhang, D.; Rudolph, N.; Woytowicz, P. Reliable Optimized Structures with High Performance Continuous Fiber Thermoplastic Composites from Additive Manufacturing (AM). In Proceedings of the SAMPE 2019, Charlotte, NC, USA, 20–23 May 2019.
- Kim, R. Dimensional stability of composite in a space thermal environment. *Compos. Sci. Technol.* **2000**, *60*, 2601–2608. [CrossRef]
- Stewart, M.C. *The Dependence of the Change in the Coefficient of Thermal Expansion of Graphite Fiber Reinforced Polyimide IM7-K3B on Microcracking due to Thermal Cycling*; NASA: Hampton, VA, USA, 1995.

18. Crowe, D.; Feinberg, A. *Design for Reliability*; CRC Press: Boca Raton, FL, USA, 2001; p. 24. ISBN 978-0-8493-1111-6.
19. Escobar, L.A.; Meeker, W.Q. A Review of Accelerated Test Models. *Stat. Sci.* **2006**, *21*, 552–577. [[CrossRef](#)]
20. Unigovski, Y.B.; Grinberg, A.; Gutman, E.M.; Shneck, R. Low-cycle Fatigue of Thermally-Cycled Carbon-Epoxy Composite. *J. Met. Mater. Miner.* **2012**, *22*, 21–30.
21. Abdullah, F.; Okuyama, K.; Fajardo, I.; Urakami, N. In Situ Measurement of Carbon Fibre/Polyether Ether Ketone Thermal Expansion in Low Earth Orbit. *Aerospace* **2020**, *7*, 35. [[CrossRef](#)]
22. Peat, C. ISS Orbit. Available online: <https://www.heavens-above.com/orbit.aspx?satid=25544> (accessed on 15 April 2020).
23. Mori, K.; Ishizawa, J. *Protection of Materials and Structures from the Space Environment*; Springer Berlin Heidelberg: Heidelberg, Germany, 2013; Volume 32, ISBN 978-3-642-30228-2.
24. Wijker, J. *Jaap. Spacecraft Structures*; Springer Berlin Heidelberg: Heidelberg, Germany, 2008; ISBN 978-3-642-09477-4.
25. Natali, M.; Torre, L. *Wiley Encyclopedia of Composites*; John Wiley & Sons, Inc.: Hoboken, NJ, USA, 2012; p. weoc045. ISBN 978-1-118-09729-8.
26. Potts, R.L. Application of integral methods to ablation charring erosion - A review. *J. Spacecr. Rockets* **1995**, *32*, 200–209. [[CrossRef](#)]
27. Miller, I.M.; Sutton, K. *An Experimental Study of the Oxidation of Graphite in High-Temperature Supersonic and Hypersonic Environments*; National Aeronautics and Space Administration: Hampton, VA, USA, 1966; p. 45.
28. Paillous, A.; Pailler, C. Degradation of multiply polymer-matrix composites induced by space environment. *Composites* **1994**, *25*, 287–295. [[CrossRef](#)]
29. Chawla, K.K. *Composite Materials*; Springer New York: New York, NY, USA, 2012; pp. 137–195. ISBN 978-0-387-74364-6.
30. Russell, D.A.; Connell, J.W.; Fogdall, L.B. Electron, Proton, and Ultraviolet Radiation Effects on Thermophysical Properties of Polymeric Films. *J. Spacecr. Rockets* **2002**, *39*, 833–838. [[CrossRef](#)]
31. Mahat, K.B.; Alarifi, I.; Alharbi, A.; Asmatulu, R. Effects of UV Light on Mechanical Properties of Carbon Fiber Reinforced PPS Thermoplastic Composites. *Macromol. Symp.* **2016**, *365*, 157–168. [[CrossRef](#)]
32. Callister, W.D.; Rethwisch, D.G. *Materials Science and Engineering*, 10th ed.; Wiley: Hoboken, NJ, USA, 2018.
33. Chivers, R.A.; Moore, D.R. The effect of molecular weight and crystallinity on the mechanical properties of injection moulded poly(aryl-ether-ether-ketone) resin. *Polymer* **1994**, *35*, 110–116. [[CrossRef](#)]
34. Kato, S.; Matsuda, S.; Okuyama, K.; Gibo, K.; Oya, H.; Watanabe, A.; Shimada, N.; Sakai, S. Study of the Effects of Heat Load, Ablator Density and Backup Structure upon the Thermal Protection Performance of Heat Shield Systems Consisting of Phenolic Carbon Ablators. *Trans. Jpn. Soc. Aeronaut. SPACE Sci. Aerosp. Technol. Jpn.* **2016**, *14*, 95–104. [[CrossRef](#)]
35. Szasz, B.A.; Okuyama, K. A New Method for Estimating the Mass Recession Rate for Ablator Systems. *Int. J. Mech. Mechatron. Eng.* **2014**, *8*, 5. [[CrossRef](#)]
36. Recovered HTV Small Re-entry Capsule was opened for media at JAXA TKSC. Available online: https://iss.jaxa.jp/en/htv/mission/htv-7/181205_interview.html (accessed on 13 January 2020).
37. Yin, T.; Zhang, Z.; Li, X.; Feng, X.; Feng, Z.; Wang, Y.; He, L.; Gong, X. Modeling ablative behavior and thermal response of carbon/carbon composites. *Comput. Mater. Sci.* **2014**, *95*, 35–40. [[CrossRef](#)]
38. Kubota, Y.; Miyamoto, O.; Aoki, T.; Ishida, Y.; Ogasawara, T.; Umezu, S. New thermal protection system using high-temperature carbon fibre-reinforced plastic sandwich panel. *Acta Astronaut.* **2019**, *160*, 519–526. [[CrossRef](#)]
39. Okuyama, K.; Kato, S.; Yamada, T.; Zako, M. Determination of thermo-chemical parameters affecting the oxidation recession of carbonized CFRP surface. *Tanso* **2004**, *213*, 128–133.
40. Barnes, J.A.; Simms, I.J.; Farrow, G.J.; Jackson, D.; Wostenholm, G.; Yates, B. Thermal expansion characteristics of PEEK composites. *J. Mater. Sci.* **1991**, *26*, 2259–2271. [[CrossRef](#)]
41. Stepashkin, A.A.; Chukov, D.I.; Senatov, F.S.; Salimon, A.I.; Korsunsky, A.M.; Kaloshkin, S.D. 3D-printed PEEK-carbon fiber (CF) composites: Structure and thermal properties. *Compos. Sci. Technol.* **2018**, *164*, 319–326. [[CrossRef](#)]
42. Duffa, G. *Ablative Thermal Protection Systems Modeling*; American Institute of Aeronautics and Astronautics: Reston, VA, USA, 2013; ISBN 978-1-62410-171-7.

43. Hasselman, D. Effect of Micro-Cracking on Thermal Conductivity: Analysis and Experiment. In *Thermal Conductivity 16*; Larsen, D.C., Ed.; Springer: Boston, MA, USA, 1983; pp. 417–431.
44. Siebeneck, H.J.; Hasselman, D.P.H.; Cleveland, J.J.; Bradt, R.C. Effects of Grain Size and Microcracking on the Thermal Diffusivity of $MgTi_2O_5$. *J. Am. Ceram. Soc.* **1977**, *60*, 336–338. [[CrossRef](#)]
45. Kato, S.; Okuyama, K.; Nishio, S.; Sakata, R.; Hama, K.; Inatani, Y. Numerical Analysis of Charring Ablation for Ablative Materials of Re-Entry Capsules. *J. Jpn. Soc. Aeronaut. SPACE Sci.* **2002**, *50*, 255–263. [[CrossRef](#)]



© 2020 by the authors. Licensee MDPI, Basel, Switzerland. This article is an open access article distributed under the terms and conditions of the Creative Commons Attribution (CC BY) license (<http://creativecommons.org/licenses/by/4.0/>).